

DENSE CORES IN DARK CLOUDS. VI. SHAPES

P. C. MYERS,¹ G. A. FULLER,¹ A. A. GOODMAN,^{1,2} AND P. J. BENSON³

Received 1990 July 23; accepted 1991 January 31

ABSTRACT

Forty-eight line intensity maps of 16 dense cores in dark clouds are compared, based on observations in the 13 mm line of NH_3 and in the 3 mm lines of CS and C^{18}O . The core maps have mean FWHM size 0.15 pc (NH_3), 0.27 pc (CS), and 0.36 pc (C^{18}O). From line to line, the maps are similar in their position on the sky, in their axial ratio 0.5–0.6, and in the alignment of their long axes, usually within 20° . Elongation is thus a common characteristic of dense cores. Therefore, cores are not generally in isolated equilibrium between self-gravity and isotropic random motions. Elongation is evident in cores with and without stars, so it precedes, rather than follows, star formation. The typical observed axial ratio can arise from identical oblate spheroids, if they are highly flattened, with axial ratio less than 0.1–0.3, or from prolate spheroids, if they are modestly elongated, with axial ratio 0.4–0.5. Six of the 16 cores are likely to be prolate because they align with, and are integral parts of, more extended structures seen in obscuration and/or CO line emission. The 10 other cores have less certain three-dimensional shape. Their elongation cannot generally arise from rotational flattening, because they lack the necessary velocity shift in magnitude, direction, or both. Their line widths, column densities, and sizes are equally consistent with virial equilibrium models of spheres, magnetized or rotating oblate spheroids, and finite segments of infinitely long prolate cylinders. The prevalence of prolate cores suggests that initial conditions for low-mass star formation should in some cases include prolate geometry. Prolate cores cannot be described by isolated equilibrium models, so models of prolate environments, and the development of prolate fragments, may be an important part of their description.

Subject headings: interstellar: molecules — nebulae: structure — stars: formation

1. INTRODUCTION

The shape of a molecular cloud core contains information on the recent history of the core's internal and external forces and motions. Analysis of core shapes is thus of interest to help describe the physical processes that form, maintain, and destroy cores, and to identify initial conditions for formation of stars.

A study of 27 dense cores in nearby dark clouds found that only four cores have maps in the $(J, K) = (1, 1)$ line of NH_3 with relative elongation greater than a factor 2 (Myers & Benson 1983). Elongation was therefore considered to be relatively unimportant. Analysis of these objects in terms of spherical models indicates that the core velocity dispersions, densities, and sizes are consistent with virial equilibrium or the early stages of collapse. Comparison with the incidence of nearby T Tauri stars and *IRAS* sources suggests that such cores form low-mass stars (Myers & Benson 1983; Beichman et al. 1986). The characteristic physical properties of these cores, apart from their shapes, have been used in models of several aspects of the formation of low-mass stars (e.g., Larson 1984, 1985; Terebey, Shu, & Cassen 1984; Adams & Shu 1985, 1986; Lizano & Shu 1989).

Several recent developments yield a much more detailed description of core shape than was previously possible. First, some of the maps discussed by Benson (1983) and by Myers & Benson (1983) have been enlarged, so that departures from

circular shape are more evident; and 14 new NH_3 maps of dense cores have been completed (Benson & Myers 1989, hereafter BM). Second, 16 of the cores studied in the ammonia line have also been mapped in the 3 mm lines of CS and C^{18}O , showing significant elongation, usually along a direction well aligned with that of the ammonia map (Fuller 1989). Third, ammonia maps of cores associated with molecular outflows show elongation in 17 of the 21 cases where the cores are resolved (Torrelles et al. 1983, 1986; Anglada et al. 1989). Fourth, maps of dark cloud filaments in the ^{13}CO line show significant elongation, and alignment of the dark filaments and the elongated line map features (Heyer et al. 1987; Loren 1989).

Thus, it is now appropriate to undertake a detailed description of dense core shapes and to analyze the implications of core shapes for core physics. In this paper, we compare maps of 16 cores in the lines of NH_3 , C^{18}O , and CS presented by BM and by Fuller (1989). Our main finding is that the three line maps of a core are generally similar in their position, in their elongation, and in their orientation, suggesting that elongation is a common characteristic of dense cores and not an artifact of peculiar excitation, chemistry, or selection, or of insufficient sample size.

This finding implies that most cores cannot be in equilibrium solely between self-gravity and isotropic random motions. Furthermore, core environments suggest that at least six cores in the sample of 16 are prolate, rather than oblate. In some cases, prolate geometry is thus an initial condition for low-mass star formation. A model prolate core, consistent with available data, is a near-equilibrium fragment of a longer self-gravitating cylinder, which may be magnetized.

Section 2 presents the observed core maps and describes their shapes; § 3 discusses the observational constraints on their possible three-dimensional shapes; and § 4 discusses the

¹ Harvard-Smithsonian Center for Astrophysics, Mail Stop 42, 60 Garden Street, Cambridge, MA 02138. G. A. F. also Astronomy Department, University of California, Berkeley.

² Astronomy Department, University of California, Campbell Hall, Berkeley, CA 94720. Also Harvard-Smithsonian Center for Astrophysics.

³ Astronomy Department, Wellesley College, Whittin Observatory, Wellesley, MA 02181.

consistency of oblate and prolate cores with core environments, and with equilibrium and near-equilibrium models. The appendix presents equations used in comparing predictions of nonspherical models with quantities derived from core observations.

2. TWO-DIMENSIONAL SHAPES OF CORE MAPS

Figure 1 presents 48 half-maximum intensity contours of 16 dense cores in nearby dark clouds, as given by BM (NH_3 line) and by Fuller (1989; CS and C^{18}O lines.) For each core, the maps have been reduced to a common scale and center coordinate. This display format allows comparison from line to line of map size, overlap, elongation, and alignment; but it omits details of internal structure, such as multiple peaks. These details can be seen in the original references.

The maps were made with FWHM angular resolution $0.75''$ (C^{18}O), $1.1''$ (CS), and $1.5''$ (NH_3), and with sampling interval $1''$, or in a few cases $2''$. At the range of core distances observed, $1''$ corresponds to $0.04\text{--}0.13$ pc. Thus all conclusions about core elongation and alignment presented here refer to size scales of about 0.1 pc, or larger. The angular coverage of each map generally extends 1 or 2 beams beyond the half-maximum contour. Therefore the relatively small NH_3 maps have less

coverage than the relatively larger CS and C^{18}O maps. A more complete comparison would require enlargement of the smaller maps, particularly in cases where a second condensation might be expected from the structure of the larger map (e.g., NH_3 in L134A and L1512; CS in L1495). All of the line observations were made with spectral resolution near 0.1 km s^{-1} , so that each spectral line width ($0.3\text{--}1.0$ km s^{-1}) is well resolved. All of the line observations were made with brightness temperature sensitivity near 0.1 K, so that each peak line intensity ($0.5\text{--}2.0$ K) is well defined.

The shapes of the maps were characterized in two similar ways. The methods are described in more detail, and their results are given, in BM and Fuller (1989). Each NH_3 line intensity map was fitted by a two-dimensional Gaussian, yielding the center position, major axis orientation, and FWHM length of the major and minor axes. Each axis length was corrected for beam broadening by subtracting the FWHM beam diameter in quadrature. The axial ratio p is the ratio of corrected minor and major axis lengths. Each CS and C^{18}O line intensity map was used to find the position of the centroid. Then the second moments of the map were calculated with respect to the centroid, and the matrix of the moments was diagonalized to find the principal axis directions. The axis

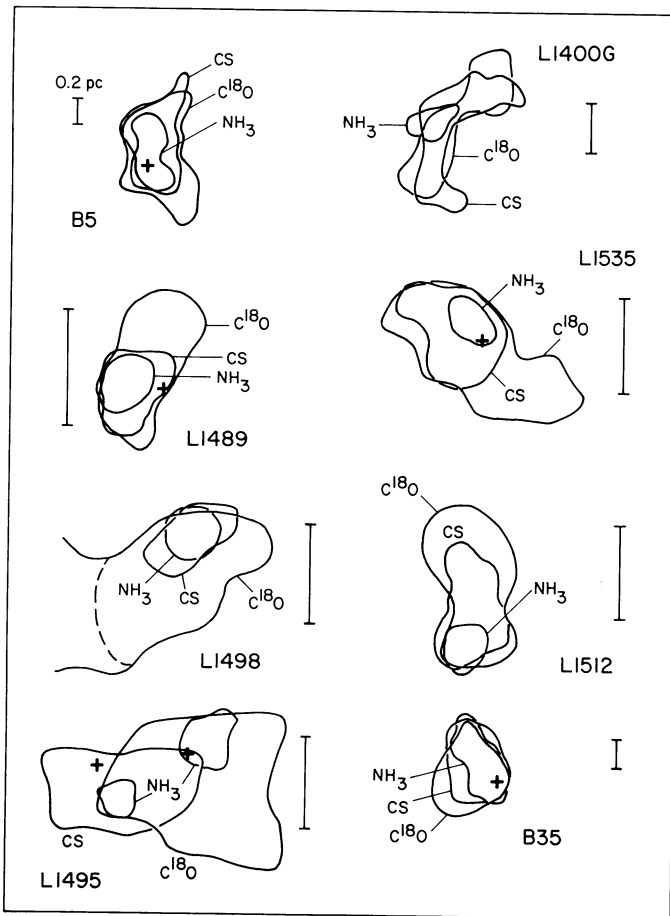


FIG. 1a

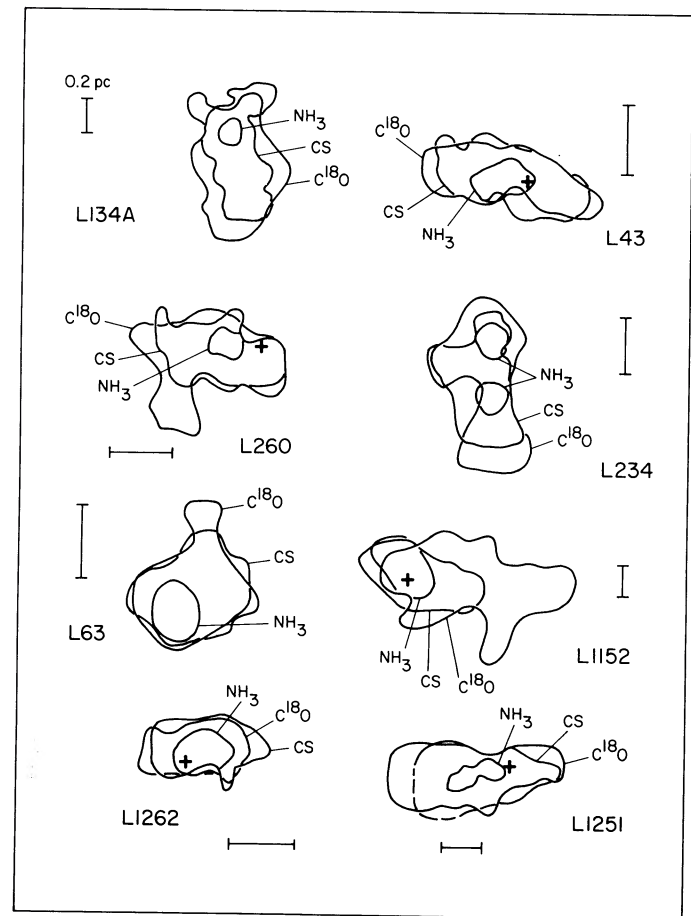


FIG. 1b

FIG. 1.—Half-maximum intensity contours of 16 dense cores in dark clouds, in the 1.3 cm $(J, K) = (1, 1)$ lines of NH_3 , from Benson & Myers (1989), and in the 3.0 mm $J = 2 \rightarrow 1$ line of CS, and the 2.7 mm $J = 1 \rightarrow 0$ line of C^{18}O , from Fuller (1989). For each map, North is up, East is left, and the linear scale 0.2 pc is indicated. A cross indicates an associated star.

lengths were obtained from the intersection of the axis directions and the HM intensity contour. The correction for beam broadening was negligible, since in comparison with the NH_3 data, the beam sizes are smaller by a factor 1.3–1.8, while the map sizes are larger by a factor ~ 2 .

Each of these methods of shape description is based on all of the map data, not just that of a single contour. The choice of the HM contour as a fiducial size is arbitrary in that the contour at, say, 0.8 or 0.2 of the maximum could also be used. But the HM contour is a good choice in the sense that for most of the maps presented here it is nearly the largest, and therefore the best resolved, contour.

The uncertainties in the map axis orientation and axial ratio were estimated by numerical simulations which match the observed maps in the ratios of axis lengths, of signal to noise, and of size to resolution. These simulations show that the standard deviations in axial ratio, σ_p ; and in position angle, σ_θ , are typically $0^\circ.04$ and 1° when $p = 0.3$; $0^\circ.04$ and 5° when $p = 0.5$; and $0^\circ.1$ and 14° when $p = 0.7$. As p increases, the contours become more nearly circular, and the position angle uncertainty σ_θ increases, as expected. For $p > 0.7$, σ_θ exceeds 14° , so that θ is too uncertain for useful comparisons of position angle.

Inspection of Figure 1 shows one prominent difference and three prominent similarities among the three line maps of each core. The maps differ in their size: the average over the maps of the geometric mean diameter of the FWHM contour of NH_3 emission, typically 0.15 pc, is about half that for CS, 0.27 pc, and the diameter for CS is typically about 0.8 of that for C^{18}O , 0.36 pc. The relative sizes of the NH_3 and C^{18}O maps can be understood in terms of the relative densities of collision partners (H_2 molecules and He atoms) needed to excite the lines: $\sim 1 \times 10^4 \text{ cm}^{-3}$ for NH_3 and $\sim 2 \times 10^3 \text{ cm}^{-3}$ for C^{18}O . In this picture, the denser gas traced by both the NH_3 line and the C^{18}O line is surrounded by less dense gas traced only by the C^{18}O line. The CS maps, however, are inconsistent with this picture: the density needed for CS line excitation exceeds that for C^{18}O by a factor of ~ 200 , yet the CS and C^{18}O map diameters typically differ only by 10%. These issues are discussed further by Fuller (1989) and by Zhou et al. (1989).

The maps are similar, first, in their location on the sky: the NH_3 contour is essentially surrounded by the CS and C^{18}O contours in 13 of 16 cases. It extends beyond the CS and/or C^{18}O contour by about 20% of its enclosed area in two cases (L1152 and L1400G), and it is completely excluded by the CS contour in one case (L1495; but improved map coverage may reduce this discrepancy, as discussed above). Further, the CS contour is enclosed by, or has substantial overlap with, the C^{18}O contour in all but two cases: L234, where about 30% of its enclosed area is excluded by the C^{18}O contour; and L1495, where about half of its enclosed area is excluded by the C^{18}O contour.

Second, the maps are similar in their relative elongation: their axial ratios have mean \pm standard error of the mean 0.55 ± 0.04 for NH_3 ,⁴ 0.59 ± 0.05 for CS, and 0.49 ± 0.05 for C^{18}O .

In three cases the map contour has a prominent spur that makes an ellipsoidal model a relatively crude approximation (C^{18}O in L260 and L234; CS in L1400G); nonetheless, these three maps also have substantial elongation, and we include them in our statistical sample.

⁴ These statistics are for the cores in Fig. 1, a subset of the BM sample. For all 41 cores in BM, the mean \pm standard error is 0.59 ± 0.03 .

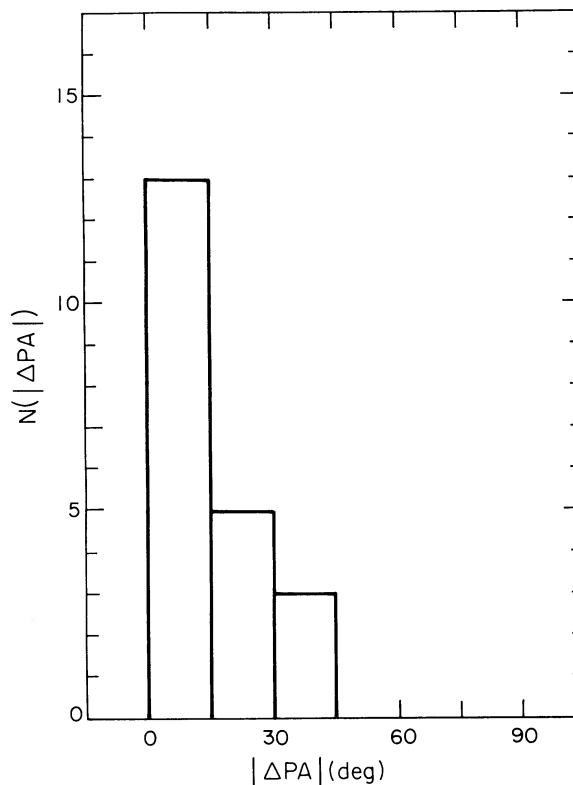


FIG. 2.—Number distribution of the absolute difference in long axis position angle for 21 map pairs of cores, where the maps have well-defined position angles. Most map pairs are well aligned.

Third, the maps are similar in the orientation of their long axes, from line to line for each core. In six cores, the CS and C^{18}O contours are nearly identical, thereby defining essentially the same long axis; in nine cores, the CS and C^{18}O contours differ in size, but have similar shape and orientation. In one core, L1495, the orientations differ substantially. The NH_3 axis orientations are not as well determined as for CS and C^{18}O , because the NH_3 maps have fewer data points and coarser angular resolution than do the CS and C^{18}O maps. Yet the alignment of a NH_3 map axis and the axes of the larger maps is generally good, when the NH_3 map is elongated enough to have a well-determined direction. To quantify the relative alignment of elongated maps, the 48 map contours in Figure 1 were modeled as ellipses, and those 36 with axial ratio less than 0.7 were judged to have a well-determined position angle. Among these 36 maps are 21 independent pairs, such as the NH_3 and C^{18}O maps of L1535. For these 21 map pairs, Figure 2 shows the number distribution of the angle between the long axes. Eighteen of the 21 pairs are aligned within 30° —a far greater fraction than would be expected to arise by chance.

In summary, the 16 dense cores in Figure 1 show significant similarity from line map to line map in their position on the sky, in their relative elongation, and in their orientation. We note that their spectral line profiles also have significant overlap from line to line for each core, further supporting the idea that all three maps are sampling largely the same volume of colocated gas. Together, these similarities suggest that the typical dense core has an elongated distribution of its total column density, with axial ratio 0.5–0.6, over size scales 0.1–0.3 pc.

3. THREE-DIMENSIONAL SHAPES OF CORES

If a dense core has an elongated distribution of column density, its distribution of number density cannot be spherically symmetric. This departure from spherical symmetry implies that the simplest and best known model of isolated core equilibrium—self-gravity against random motions—cannot account for observed core shapes (BM). To better define the forces needed to break spherical symmetry, it is necessary to constrain the three-dimensional shape which corresponds to the elongated maps described above in § 2.

The two-dimensional core maps on § 2 may arise from a variety of three-dimensional structures. To allow a more definite conclusion, we assume that the observed core maps are projections on the plane of the sky of spheroids, that is, geometrical figures constructed by rotating an ellipse about its major axis (prolate spheroid) or about its minor axis (oblate spheroid). Each such spheroid has nested surfaces of constant density, assumed to have identical shape. The shape of a spheroid is described by the axial ratio q , the ratio of the smaller and larger of the principal axes of a constant-density surface. The projection of the spheroid on the plane of the sky has nested contours of constant column density. These contours are then ellipses of identical shape. This shape is described by the projected axial ratio p , the ratio of the smaller and larger principal axes of an ellipse of constant column density. Because of foreshortening, $p \geq q$.

If the distribution of true axial ratios q is known, and if the distribution of symmetry axis directions in space is also known, one can predict the expected distribution of projected axial ratios for the prolate and oblate cases. Conversely, given the observed distribution of p , one can infer information about the expected distribution of true axial ratios q_o if the cores are oblate, or the expected distribution of true axial ratios q_p if they are prolate. The probability distributions which relate p and q_p , and p and q_o , have been discussed by Fall & Frenk (1983), among others, in the context of estimating the three-dimensional shapes of elliptical galaxies and globular clusters.

We assume for simplicity that the spheroidal cores are either all prolate or all oblate, and that the cores are identical, except for the orientation of their symmetry axes in space, which has an isotropic distribution of probability. For both the oblate and prolate cases, the probability density with respect to p falls monotonically from its maximum value at $p = q$ to its minimum value at $p = 1$. For a given value of q , the oblate distribution is more nearly uniform, while the prolate distribution is more concentrated near $p = q$.

The mean of the NH_3 , CS, and C^{18}O distributions of p is asymmetric in the sense expected from a single value of q , but its asymmetry is not pronounced enough, suggesting that a distribution of values of q is needed, concentrated near $q = \langle p \rangle$. However, the data are too few to define this distribution clearly. Instead we idealize the problem further and compare the mean observed axial ratio $\langle p \rangle$ with the values expected for oblate and prolate model spheroids. Integration over the distributions given by Fall & Frenk (1983) yields

$$\langle p \rangle = \frac{1}{2} \left[1 + \frac{q_o^2}{(1 - q_o^2)^{1/2}} \ln \frac{1 + (1 - q_o^2)^{1/2}}{q_o} \right] \quad (1)$$

for oblate spheroids, and

$$\langle p \rangle = \frac{q_p}{(1 - q_p^2)^{1/2}} \arccos q_p \quad (2)$$

for prolate spheroids.

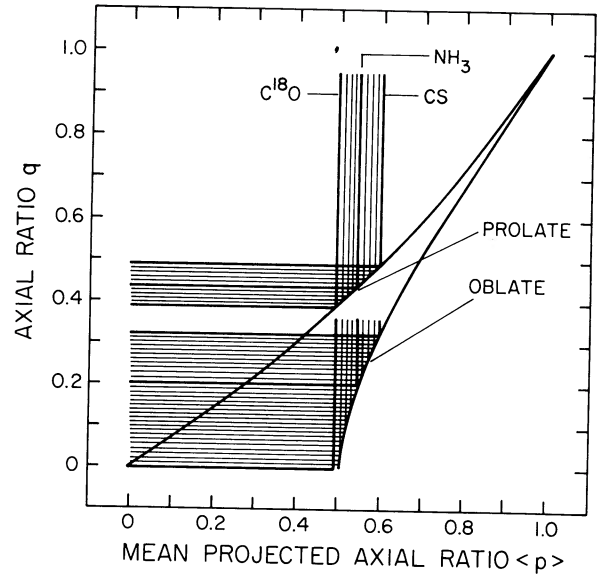


FIG. 3.—Plots of the axial ratio q of an ensemble of identical spheroids having an isotropic distribution of symmetry axis orientations, against $\langle p \rangle$, the mean of their distribution of projected axial ratios, for prolate and oblate spheroids. The heavy vertical lines show observed values of $\langle p \rangle$ for the 16 cores mapped in spectral lines of NH_3 , CS, and C^{18}O . Vertical shading shows the range of observed values. Heavy horizontal lines show model values of q required for consistency with the observed values of $\langle p \rangle$. Horizontal shading shows the range of allowed values of q for each shape: for oblate spheroids, $\langle p \rangle < 0.1-0.3$, indicating substantial flattening; for prolate spheroids, $0.4-0.5$, indicating modest elongation.

Figure 3 shows plots of q_p and q_o versus $\langle p \rangle$, obtained from equations (1) and (2). It shows that for both prolate and oblate spheroids, the mean projected axial ratio is at least as great as the true axial ratio. For prolate spheroids, the projected axial ratio is only slightly greater than the true ratio, while for oblate spheroids, the projected ratio is substantially greater than the true ratio. These properties can be understood by noting that the projected axial ratio ranges from q , when the projected short and long axes equal the true short and long axes, to unity, when the symmetry axis lies along the line of sight. Thus the mean projected ratio $\langle p \rangle$ contains no contributions smaller than q , so $\langle p \rangle$ must equal or exceed q . Moreover, for the same true axial ratio q , oblate spheroids have a larger mean projected ratio $\langle p \rangle$ than do prolate spheroids, because the contribution of projected axial ratios near unity to the mean projected ratio has a greater weight for oblate than for prolate spheroids.

Figure 3 also shows the mean axial ratio observed for the NH_3 , CS, and C^{18}O cores described in § 2. The range of means is about twice the standard error, so we adopt this range as representative of the observed core axial ratios. Comparison of this range with the curves in Figure 3 indicates that if the cores are modeled as prolate spheroids, their true axial ratio must be $q_p = 0.4-0.5$; but if they are oblate, their axial ratio q_o ranges from less than 0.1 to 0.3. (Formally, when $\langle p \rangle$ is as low as 0.49, as derived from the C^{18}O maps, $\langle p \rangle$ is inconsistent with any oblate spheroid; but the standard error implies some likelihood that $\langle p \rangle$ is slightly greater than 0.50, so we write the low end of the range of q_o as < 0.1 .) This result implies that if observed cores are prolate spheroids, their necessary relative elongation is relatively modest; while if they are oblate, their required relative flattening is much more extreme.

The foregoing model assumes that all the prolate spheroids have the same axial ratio, and that all the oblate spheroids have another identical axial ratio. If, as seems more realistic, each type of spheroid has a distribution of axial ratios, the difference between prolate and oblate axial ratios required for consistency with observations will probably be reduced. Nevertheless, this result suggests that a significant number of dense cores may be prolate, rather than oblate. This model also assumes that all orientations of the spheroid symmetry axis are equally probable—which could be false if many of the cores were in the same complex, and if their long axis directions were correlated. But then their projected long axis directions would also be correlated, whereas inspection of the five maps of Taurus cores in Figure 1 shows no significant correlation among the axis directions.

4. DISCUSSION

4.1. Comparison with Other Observations

The description in § 2 is based on the substantial similarity in position angle and axial ratio among maps of NH_3 , CS, and C^{18}O line emission in 16 dense cores. However, this degree of similarity is not always evident when other cores and/or other lines are considered. The emission in lines of CS, C^{18}O , NH_3 , SO, C_3H_2 , and H^{13}CO^+ , mapped in L183 by Swade (1989), illustrate this point. There the CS and C^{18}O maps have similar location, size, axial ratio, and major axis orientation along a SE-NW line. However, the NH_3 map is elongated in the N-S direction so that its southern emission peak coincides approximately with those of CS and C^{18}O , while its northern peak lies outside the lowest CS and C^{18}O contours. In this property the NH_3 map resembles the C_3H_2 and H^{13}CO^+ maps. Thus the NH_3 map disagrees with the CS and C^{18}O maps, but agrees with two others in its long axis orientation.

These displacements in map contours from lines of one molecule to another probably reflect molecular abundance variations. They appear not to occur at random, but rather in groups of lines, so that the spatial variation within a group is smaller than from group to group. These variations make it especially desirable to compare a relatively large sample of core maps before drawing conclusions about their characteristic shapes.

The general consistency of core maps from line to line for the dense cores discussed here contrasts with the diversity of core maps seen toward regions of massive star formation. This diversity is marked when the spatial resolution is comparable to, or finer than, the typical resolution 0.05 pc in Figure 1. For example, Hat Creek interferometer maps of the Orion molecular cloud show strong emission from the Kleinmann-Low nebula in 3 mm lines of HC_3N , CH_3OH , OCS, and SO_2 ; but 0.05 pc away, “continuum source 1” shows emission only from HC_3N and CH_3OH , and not from OCS and SO_2 (Plambeck 1988). The increased map diversity in regions with massive stars is generally attributed to increased variation in molecular abundance, due perhaps to the relatively large role of shocks and ionizing photons in regions with massive stars.

The elongation of ammonia maps of cores presented in § 2 is generally consistent with the elongation reported by Torrelles et al. (1983, 1986) and Anglada et al. (1989), in that nearly all resolved cores are elongated by a significant factor, with the axial ratio for 19 cores having mean \pm standard error of the mean 0.58 ± 0.05 . The difference between means of the Torrelles et al. sample and the BM sample is therefore statistically insignificant.

The consistency of axial ratios for these two sets of ammonia maps implies that the core axial ratio does not depend significantly on the differing properties of stars and stellar winds in the two samples. For the 21 BM cores having no star within one FWHM map diameter of the map peak, and for the 20 cores having a star within one map diameter, the axial ratio has mean \pm standard error 0.59 ± 0.03 in each case. Thus, presence or absence of an associated star makes no difference to the mean axial ratio of the core. Similarly, comparison of the samples of Torrelles et al. (1983, 1986) and Anglada et al. (1989) and of BM indicates no significant difference in mean axial ratio for cores with and without CO outflow, and no significant difference for cores with associated stars of low ($0.3\text{--}30 L_\odot$) or high ($30\text{--}10^4 L_\odot$) luminosity. Thus, for the cores considered here, core elongation is unlikely to be a consequence of star formation or outflows, as is sometimes suggested. Rather, core elongation would seem to be an initial condition, which precedes star formation.

A comparison of map overlap similar to that in § 2 was carried out by Zhou et al. (1989) for 10 cores, seven of which are also presented in this paper. As in § 2 most of the maps show significant overlap of their half-maximum contours. Zhou et al. also point out that the peak positions of the NH_3 and CS maps of a core generally differ by $1\text{--}2'$.

4.2. Core Environments

Perhaps the most decisive consideration for determining characteristic core shapes is the structure of the extended gas and dust associated with many cores. For the 16 cores discussed in this paper, we have carefully examined the Palomar Sky Atlas red prints to estimate the size, shape, and direction of elongation of the associated visible obscuration. This visible obscuration extends from the visually opaque region (where no background stars are visible) to the lightly obscured periphery of the dark cloud, where the visual extinction is about 1 mag, and where it is difficult to separate the cloud from its background. For 14 of the 16 cores, the visually opaque obscuration is approximately coincident with the location, relative elongation, and long axis orientation indicated by the maps in Figure 1. For the other two cores, in B5 and L1495, the opaque obscuration is too extended and complex in shape to allow a match to the core maps. Of the 14 cores with coincident opaque obscuration, their more extended obscuration can be divided into three groups:

1. *Isolated globules.*—These six objects (L1489, L1512, L134A, L63, L1152, L1262) have visible obscuration 1–3 times the extent of the opaque obscuration. Their elongation has about the same axial ratio and direction as indicated by the core maps. They appear unconnected to any other obscuration, although two are located near the western (L1489) and eastern (L1512) edges of the Taurus complex.

2. *Parts of complex filaments.*—These five objects (L1498, L1400G, L1535, L234, L260) lie in filamentary structures whose overall length is 10–30 times that of the individual dark cloud that contains the core. The filaments are “complex” in that they contain faint multiple branches (L1498), or in that their obscuration is not continuous, but rather has distinct gaps. Such segmented structures were called “globular filaments” by Schneider & Elmegreen (1979). In their notation, L1535 is GF 16 E; L234 is GF 3 Bb; and L260 is GF 3 C3.

3. *Parts of simple filaments.*—These three objects (B35, L43, L1251) are highly elongated continuous structures, with relatively little branching or segmentation. Their length is again of order 10 times that of the core map, and the direction of core

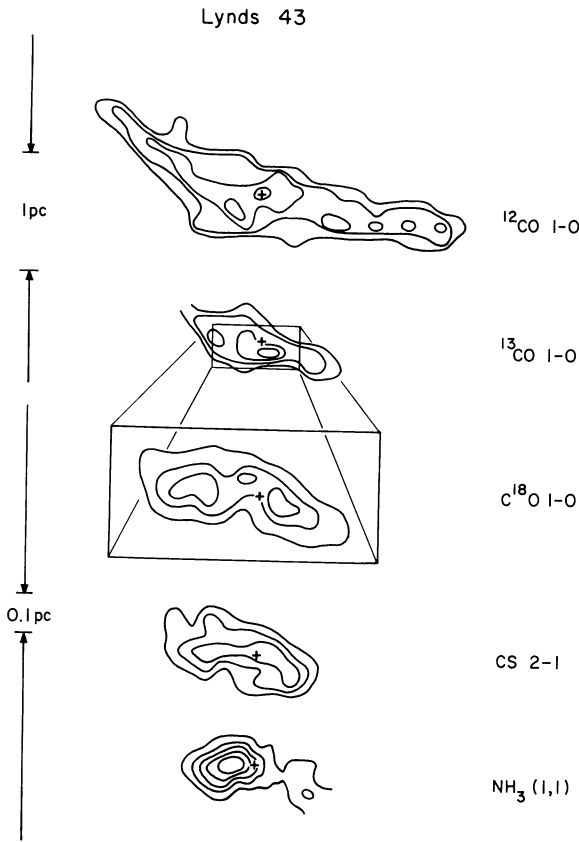


FIG. 4.—Maps of line intensity from the simple filamentary cloud Lynds 43, in ^{12}CO and ^{13}CO (Elmegreen & Elmegreen 1978); C^{18}O and CS (Fuller 1989); and NH_3 (Benson & Myers 1989). Each map has uniform contour intervals. The maps show similar orientation over more than a decade of size scale.

elongation lies along the direction of the filament. Other examples are given in Table 1 of Schneider & Elmegreen (1979), who call them “undifferentiated filaments.”

These three types of structure indicated by visual obscuration are also evident in some maps of emission from the $1 \rightarrow 0$ rotational lines of ^{12}CO and ^{13}CO . Figure 4 shows the simple filament L43, in contours of emission from lines of ^{12}CO , ^{13}CO , C^{18}O , CS, and NH_3 . As one progresses from the smallest map (NH_3) to the largest map (^{12}CO), the orientation of the long axis remains approximately constant. But the long dimension grows faster than does the short dimension, so the half-maximum contour of the NH_3 map has projected axial ratio $p \sim 0.5$, while that of the ^{12}CO map has $p \sim 0.1$. Other small-axial-ratio filaments are evident in ^{13}CO maps in Ophiuchus (Loren 1989) and Taurus (Duvert, Cernicharo, & Baudry 1986; Heyer et al. 1987). These ^{13}CO filaments closely match the structure seen in visual obscuration.

There is little doubt that the simple filaments with projected axial ratio $p \sim 0.1$, surrounding some cores, are prolate objects. Figure 3 shows that an ensemble of identical oblate spheroids cannot have a typical value of p much lower than 0.5, while prolate spheroids have no such limit. An isolated elongated dark lane might be considered as a rare instance of a highly flattened sheet seen nearly edge-on. But the presence of several such lanes in Taurus, Ophiuchus, and other regions, with nearly parallel orientations on the sky, makes such an

oblate interpretation very implausible. Indeed, dark cloud filaments are almost always considered prolate. For example, Jones & Herbig (1979) modeled the extinction in Taurus as arising from 28 prolate cylinders.

Since a simple filament with axial ratio near 0.1 is almost certainly prolate, its elongated segments seen in molecular line maps are probably also prolate, if their long axes are approximately aligned with that of the filament. The segments are then simply prolate pieces of the filament. Similarly, a complex filament with axial ratio near 0.1 is almost certainly prolate, and its separated segments are probably also prolate if they are elongated and approximately aligned with the axis of the parent structure. The elongated segments could plausibly be oblate, if their long axes were perpendicular to that of the filament, as in a stack of coins. Such a situation is expected if magnetized prolate cores collapse along their field lines (e.g., Tomisaka, Ikeuchi, and Nakamura 1988a, b; hereafter TINA, b; Lizano & Shu 1989). However, molecular line observations of well-defined perpendicular segments have not been reported, and most of the elongated segments in the photographs presented by Schneider & Elmegreen (1979) are more nearly parallel than perpendicular to the long axis of the parent filament.

These considerations indicate that cores in simple filaments (B35, L43, and L1251) are most certainly prolate; and cores having approximately the same orientation as the complex filaments to which they belong (L234, L1535, L1400 G) are probably prolate. These six cores have maps slightly more elongated than the others—another indication that they are prolate: they include the four smallest axial ratios in the sample, $p = 0.20\text{--}0.28$. Furthermore, the eight other elongated cores in Figure 1 that lack filamentary extensions in visual obscuration are not necessarily excluded from being prolate—rather, they lack decisive evidence.

The cores identified as prolate in this paper join several other cores having evidence of prolate shape. TMC-1 (Churchwell, Winnewisser, & Walmsley 1978) and TMC-1C (Benson & Myers 1983) are each elongated in NH_3 and C^{18}O maps, with axial ratio ~ 0.2 , and each of their long axes is approximately parallel to the long axis of the dark cloud that contains them, Heiles Cloud 2. Also, the “Orion ridge” lies along the axis of the much more extended Orion A cloud seen in lines of ^{12}CO and ^{13}CO (Genzel & Stutzki 1989). As more molecular line maps are made in regions with filamentary large-scale structure, it is likely that more examples of prolate cores will be found.

Another aspect of core environments is the direction of optical polarization of background stars, generally attributed to the alignment of elongated dust grains by the ambient magnetic field. This direction is known for some of the cores in the present sample. Unfortunately, this knowledge does not help decide between oblate and prolate shapes, because either shape can have its symmetry axis along the magnetic field, as discussed in § 4.3. Furthermore, some dark cloud filaments that are clearly prolate are well aligned with the local direction of optical polarization, such as L1755, while others are nearly perpendicular, such as B216, and still others lie at intermediate angles (Goodman et al. 1990a). Therefore, the contribution of optical polarization directions to the question of core shapes is at present inconclusive.

4.3. Comparison with Equilibrium Models

We have compared three observable core properties—size R , line width Δv , and column density N —with predictions of

TABLE 1
EQUILIBRIUM MODELS OF ISOTHERMAL CORES WITH VARIOUS SHAPES

A. (SPHERE ($p = 1$))							
q	f	NH_3 Core ^a n (10^4 cm^{-3})	C^{18}O Core ^b n (10^4 cm^{-3})				
0	$\pi/5$	3.7	1.4				
1	$2\pi/9$	3.4	1.3				
2	$\pi/3$	2.2	0.86				
2 (SIS)	$\pi/2$	1.5	0.58				

B. ROTATING OBLATE SPHEROID ($p = 0.5$)							
q	$\epsilon_{\text{rot}}/\epsilon_{\text{therm}}$	n_c/n_0	f	NH_3 CORE ^a		C^{18}O CORE ^b	
				n (10^4 cm^{-3})	v_{shift} (km s^{-1})	n (10^4 cm^{-3})	v_{shift} (km s^{-1})
0.15	1.49	300	0.41	13	0.73	5.2	1.09
0.18	0.99	10	0.49	9.3	0.73	3.6	1.09
0.23	0.54	3	0.78	4.6	0.74	1.8	1.10
0.26	0.34	2	1.10	2.9	0.75	1.1	1.11

C. MAGNETIC OBLATE SPHEROID ($\epsilon_{\text{mag}}/\epsilon_{\text{therm}} = 1, p = 0.5$)						
q	n_c/n_0	f	NH_3 CORE ^a		C^{18}O CORE ^b	
			n (10^4 cm^{-3})	B_{\parallel} (μG)	n (10^4 cm^{-3})	B_{\parallel} (μG)
0.18	100	0.51	9.0	14	3.5	13
0.23	2	1.02	3.5	15	1.3	14
0.25	10	0.57	5.8	14	2.3	13
0.27	5	0.67	4.6	14	1.8	13

D. FINITE SEGMENT OF AN INFINITE PROLATE CYLINDER						
q	p	f	NH_3 CORE ^a		C^{18}O CORE ^b	
			n (10^4 cm^{-3})	B_{\parallel} (μG)	n (10^4 cm^{-3})	B_{\parallel} (μG)
0.4	0.5	0.88	1.5	6.2	0.56	11

^a Assuming representative values $\Delta v = 0.49 \text{ km s}^{-1}$ and $R = 0.075 \text{ pc}$.

^b Assuming representative values $\Delta v = 0.73 \text{ km s}^{-1}$ and $R = 0.18 \text{ pc}$.

stable, self-gravitating, isothermal equilibrium models of cores having either spherical, oblate, or prolate shape. These comparisons are summarized in Table 1 and in Figure 5. They indicate that the three observable quantities are mutually consistent with each of the equilibrium models; they do not clearly favor one shape over another.

We define the core radius R for a map in a particular line as the geometric mean of the largest and smallest radii of the half-maximum intensity contour. Note that this R is half that used in Myers & Benson (1983), BM, and some other papers. We make this change in notation to compare measured and model radii more conveniently and accurately. The core line width Δv is the expected FWHM of the distribution of line-of-sight velocities of the particle of mean mass, $m = 2.33 \text{ amu}$. We obtain Δv from the observed FWHM of a line, Δv_{obs} , emitted by molecules of mass m_{obs} , according to

$$\Delta v^2 = \Delta v_{\text{obs}}^2 + 8 \ln 2kT(m^{-1} - m_{\text{obs}}^{-1}), \quad (3)$$

where k is Boltzmann's constant, and T is the kinetic temperature. The motions in Δv are assumed to be random and isotropic, exerting a supporting pressure. Since the nonthermal

contribution to Δv_{obs} varies from line to line, Δv also varies from line to line.

We define N as the mean column density of gas within the HM contour of a particular map. We obtain N from the C^{18}O data of Fuller (1989) by adopting an excitation temperature of 10 K for the observed transition and for the partition function. We adopt a linear relation between C^{18}O column density and visual extinction as in Fuller's Table 4.5. We assume the usual relation between hydrogen gas column density and dust extinction (Bohlin, Savage, & Drake 1978), and we assume that the interstellar gas contains 10% He. The typical ratio of $N(\text{C}^{18}\text{O})$ to N is then 2.0×10^{-7} . We obtain N from the NH_3 data of BM in a manner similar to that for C^{18}O , as explained by BM, and by constraining the intercept of the linear relation between N and the NH_3 column density so that the mean value of N derived from the NH_3 data for the 16 clouds in this paper is the same as the mean value of N derived from the C^{18}O data. The typical ratio of $N(\text{NH}_3)$ to N is then 1.5×10^{-7} . As BM do not report the mean NH_3 column density within the HM contour, we multiply the peak NH_3 column density within a map, from their Table 7, by 0.67, a correction factor derived from the mean and peak C^{18}O column densities given in Fuller (1989).

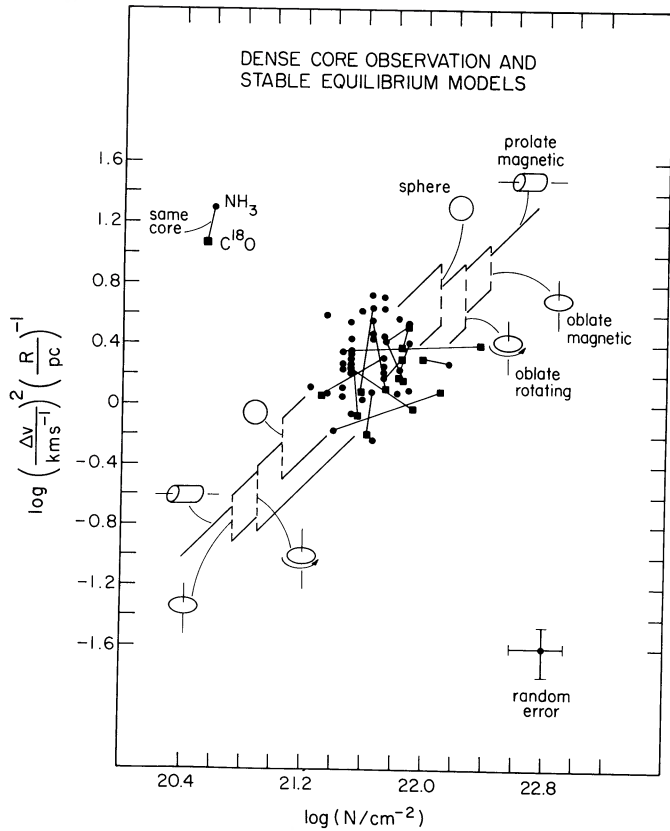


FIG. 5.—Log-log comparison of $C^{18}O$ and NH_3 dense core data with equilibrium models for various core shapes. The horizontal axis shows the mean column density over a core N , based on observed column density of $C^{18}O$ (circles) or NH_3 (squares). The vertical axis shows $\Delta v^2/R$, where Δv is the FWHM line width of the particle of mean mass, based on the line width of $C^{18}O$ or NH_3 , and R is the HWHM size of the $C^{18}O$ or NH_3 map. Data points based on NH_3 and $C^{18}O$ observations of the same core are joined by a solid line. Each equilibrium model is indicated by a solid line of unit slope, with a break near the center of the figure to avoid confusion with the data points. For the spherical and oblate spheroidal models, several possible cases were considered (see Table 1). The resulting range of intercepts is indicated by a dashed vertical line joining the solid lines of largest and smallest intercept. The models for spherical cores, oblate rotating cores, oblate magnetic cores, and segments of prolate cylinders all fit the data within its scatter.

The foregoing procedure assigns the same total column density N to two line maps of the same core, rather than the more common practice of dividing each tracer-molecule column density by an abundance ratio based on other observations. We adopt the present procedure because it is based on the same premise as the abundance-division method and is probably more accurate. Abundance determinations are usually based on star counts or color excesses to determine the visual extinction, and thus the total column density in a region. The “abundance” is then the ratio of the molecular column density derived from the tracer line observations, to the total column density. If such an abundance determination were made for each core, each tracer-line observation of that core would by definition correspond to the same total column density. Such abundance determinations are available only for a few regions; they show some variation from cloud to cloud, and they also have uncertainty due to sampling and measurement error. Therefore we use a method which enforces the equality of total column density and minimizes the propaga-

tion of error from the abundance determinations in other clouds.

One could also obtain N from R and from the density of collision partners needed for NH_3 line excitation, but this method gives a dispersion in values of N larger than that based on the adopted method.

For each of 42 NH_3 cores and 14 $C^{18}O$ cores, Figure 5 shows the quantity $(\Delta v)^2/R$ plotted against N in a log-log plot, in order to compare the observed data with predictions of equilibrium models of various shapes. A similar plot was presented by Keto & Myers (1986). The plot format is convenient because equilibrium model predictions appear as straight lines. The NH_3 and $C^{18}O$ data in Figure 5 show no significant trend, with each group of points ranging from about $(\Delta v)^2/R = 0.6$ to $5 \text{ km}^2 \text{ s}^{-2} \text{ pc}^{-1}$, and with $N = 2\text{--}16 \times 10^{21} \text{ cm}^{-2}$. The $C^{18}O$ data show somewhat greater scatter at the high end of the column density range.

All of the equilibrium models considered here require

$$\frac{(\Delta v)^2}{R} = 8 \ln 2mGnf, \quad (4)$$

where G is the gravitational constant, and where the dimensionless quantity f depends on the model. Table 1 gives the value of f for each model considered, and Figure 5 shows the range of values of f for each shape. The following paragraphs and the Appendix describe how f and the other entries in Table 1 are obtained.

For a sphere whose density n varies with radius r as r^{-s} , equality of the kinetic energy and gravitational potential energy terms of the virial theorem implies

$$f = \frac{\pi}{3} \frac{3-s}{5-2s}, \quad (5)$$

while for a singular isothermal sphere (hereafter SIS; Shu 1977), $f = \pi/2$. Figure 5 shows that spherical models with $s = 0, 1,$ and $2,$ and the SIS model, all have reasonable agreement with the observed values of $\Delta v, N,$ and R . Table 1A also lists the mean density n over a model core with $\Delta v = 0.49 \text{ km s}^{-1}$ and $R = 0.075 \text{ pc}$, typical for NH_3 cores, and with $\Delta v = 0.73 \text{ km s}^{-1}$ and $R = 0.18 \text{ pc}$, typical for $C^{18}O$ cores. We obtain this mean density from the geometry of a sphere and from equation (4),

$$n = \frac{3N}{4R} = \frac{3}{32 \ln 2mGf} \left(\frac{\Delta v}{R} \right)^2. \quad (6)$$

The resulting values, $n = 2\text{--}4 \times 10^4 \text{ cm}^{-3}$ for NH_3 cores and $0.8\text{--}2 \times 10^4 \text{ cm}^{-3}$ for $C^{18}O$ cores, are in good accord with excitation requirements (BM; Fuller 1989). On the other hand, these spherical models are inconsistent with the typical elongated core map shape, as discussed in § 3.

To compare the observed data with rotating oblate core models, we use the axisymmetric, nonmagnetic, self-gravitating, isothermal core models of Kiguchi et al. (1987; hereafter KNMH), which extend the earlier work of Stahler (1983). These calculations indicate that stable, centrally condensed structures can have substantial flattening. We consider the 11 KNMH models with oblate shape, stable equilibrium, and true axial ratio $q = 0.15\text{--}0.30$, as required by the results of § 3. Calculation of f is explained in the Appendix. Table 1B lists four representative cases. The range of f corresponds to variations in the relative rotational energy $\epsilon_{\text{rot}}/\epsilon_{\text{therm}}$, and in the degree of central concentration, also listed in Table 1B. As with

the spherical models, this range of oblate models agrees with the line width, size, and column density data shown in Figure 5. Also, the model mean density listed in Table 1B agrees within uncertainty with that needed for line excitation in the typical NH_3 and C^{18}O core.

However, these rotating models also predict a continuous shift in the line center velocity along the projected long axis. We list in Table 1B the magnitude of this shift from one edge of the core map to the other, v_{shift} , whose calculation is explained in the Appendix. The expected values of v_{shift} are $0.73\text{--}0.75\text{ km s}^{-1}$ for NH_3 cores and $1.09\text{--}1.11\text{ km s}^{-1}$ for C^{18}O cores. Velocity shifts in these ranges, and in the long axis direction, are occasionally seen in NH_3 and C^{18}O cores (Goodman et al. 1990b; Fuller 1989), such as in L43 and L1251. But they are relatively rare in core observations, suggesting that rotation is not common enough to explain the characteristic elongation of core maps. A similar conclusion was found by Arquilla & Goldsmith (1986), who found that only three of eight clouds studied in the $J = 1\text{--}0$ line of ^{13}CO have significant evidence for rotation.

To compare the observed data with oblate magnetic core models, we use the nonrotating isothermal models of TINa, b, which extend and complement earlier work by Mouschovias (1976a, b), Nakano (1984) and Lizano & Shu (1989). Like the rotating models of KNMH, these magnetic models of TINa, b show that highly flattened, stable equilibrium configurations are possible. We consider TINb models 5a–5e, which have $q = 0.15\text{--}0.30$ and stable equilibrium. These models assume equal magnetic and thermal energy density. Figure 5 shows the range of values of f , calculated as explained in the Appendix. Table 1C lists four representative cases spanning this range in f , corresponding to a range in central concentration of a factor of 50, also detailed in Table 1C. The mean densities are similar to those for the spherical and oblate rotating models. The line-of-sight component of magnetic field strength at the core boundary, suitable for comparison with measurements of the Zeeman effect, is calculated according to expression (A11). The resulting values of NH_3 and C^{18}O cores, $13\text{--}15\text{ }\mu\text{G}$, are not excluded by the few available measurements of magnetic field strength in low-mass cores. Goodman et al. (1989) found $B_{\parallel} = 19 \pm 3\text{ }\mu\text{G}$ in the dark cloud Barnard 1, using a beam large enough to enclose the HM intensity contour of OH line emission. Using the observed values of Δv and R for that cloud, and the model parameters corresponding to $q = 0.25$ in Table 1C, equation (A11) predicts $B_{\parallel} = 11\text{ }\mu\text{G}$. However, many more measurements are needed to properly test the predicted values of B_{\parallel} .

In contrast to the oblate equilibrium models considered here, no prolate equilibrium model exists, unless the pressure along the symmetry axis significantly exceeds the pressure perpendicular to the symmetry axis—a situation difficult to envision physically. Instead, we consider a finite segment of an infinitely long cylinder, which has stable and unstable equilibrium solutions, for magnetized gas having uniform temperature and Alfvén speed, with magnetic field direction along the cylinder axis (Stodolkiewicz 1963). The nonmagnetic isothermal cylinder (Ostriker 1964) is then a special case with zero Alfvén speed. For comparison with observations we define the projected $b_{1/2}$ as the value of b where the column density is half its maximum value. We consider a segment whose length along the axis is $5.0b_{1/2}$. We choose this length because it corresponds approximately to an axial ratio $q = 0.4$, which is the value indicated in § 3 for a prolate spheroid that matches the

observed projected ratio $p = 0.5$. This length also has physical significance because it is characteristic of the fastest growing unstable mode of axial fragmentation of the cylinder (Larson 1985; Bastien 1983; Stodolkiewicz 1963; Rouleau & Bastien 1990). Thus prolate cores might be consistent with marginally unstable fragments of longer cylinders.

For this prolate model, we list in Table 1D values of f , n , and B_{\parallel} calculated according to equations (A15), (A17), and (A18). As for the oblate models, these values agree reasonably well with the data considered here, as shown in Figure 5. The line-of-sight field strength for a core with $p = 0.5$, $q = 0.4$, and typical line width and size revealed by NH_3 data is $6\text{ }\mu\text{G}$; for C^{18}O data, $11\text{ }\mu\text{G}$, and for the OH data reported by Goodman et al. (1989) for B1, $14\text{ }\mu\text{G}$. Thus, among the four models considered, the sphere can be ruled out on the basis of map shape, and the rotating oblate spheroid can be ruled out on the basis of velocity shift. Neither the magnetic oblate spheroid nor the magnetic prolate cylinder segment can be ruled out by the equilibrium models in this section.

For the cores likely to be prolate because they are parts of more extended filamentary clouds, the cylinder segment model discussed here appears consistent with core shape, and with equilibrium relations among Δv , N , and R . However, the segment length may present a problem: if the cylinder is to be stable, it must be infinitely long; if it has a length consistent with observations, it is unstable. In the absence of retarding forces, it should then collapse on a dynamical time scale. In that case, such segments might not be expected to be as common as is indicated by the analysis of § 3. Further studies of the dynamical evolution of cylindrical structures are needed.

4.4. Implications

The foregoing results suggest that at least six of the 16 cores studied here have prolate shape. The remaining 10 cores have less certain shapes. If they are typically oblate, they are probably highly flattened, with typical axial ratio $q \sim 0.2$, and they are probably supported magnetically rather than rotationally in the radial direction. If some of the 10 cores with uncertain shape are prolate, they join the six more likely to be prolate in having the following properties: (1) They are modestly elongated on the 0.1 pc size scale, with typical axial ratio $q \sim 0.4$. (2) Their shape is inconsistent with models of isolated equilibrium between gravity and rotation, or between gravity and magnetic pressure. (3) Their shape, velocity dispersion, column density, and size are consistent with those of an axially unstable fragment of a self-gravitating, isothermal cylinder. (4) If the core is magnetized along the symmetry axis with uniform Alfvén speed, the line-of-sight component of the magnetic field is typically $6\text{--}11\text{ }\mu\text{G}$ —a value that appears consistent with the few relevant measurements and upper limits now available.

The prevalence of prolate cores carries several implications for our understanding of core evolution and the physics of star formation. Prolate cores are known with and without young embedded stars, and some prolate cores are parts of much larger structures, with few stars. Thus prolate shape is evidently not a consequence of star formation. Rather it appears that prolate shape is an aspect of the “initial conditions” of the formation of some stars. These initial conditions may also need to account for the forces giving rise to the prolate geometry—presumably some combination of gravitational, magnetic, and fluid forces. If the prolate core is aligned with an energetically significant magnetic field, the calculations of TIN and of

Lizano & Shu (1989) predict that the core will develop an oblate condensed structure as matter travels toward the center of mass along field lines. If this predicted outcome occurs, it must occur at a later time or on a smaller size scale than is indicated by the current observations.

Prolate initial conditions may favor the formation of binary stars—long a difficulty of models based on spherically symmetric initial conditions. Rouleau & Bastien (1990) find from numerical simulations that a self-gravitating polytrope with cylindrical symmetry will collapse into two fragments, which then fall toward their common center, provided the initial axial ratio is less than 0.6 and the initial ratio of gravitational to thermal energy is greater than a value between 1 and 2, depending on the polytropic index. Related ideas are also discussed by Boss (1988) and Zinnecker (1984, 1989).

A tendency for the axis of a molecular outflow to lie nearly perpendicular to the long axis of its associated ammonia core has been noted by Torrelles et al. (1983, 1986) and Anglada et al. (1989). Many authors have interpreted this tendency by assuming that the core is oblate. Then the outflow axis is approximately aligned with the symmetry axis of the core, as expected if the outflow axis direction is tied in a causal way to the magnetic or rotational axis of the oblate core. But this picture changes if the core is prolate: then the outflow emerges approximately perpendicular to the symmetry axis, and it is less clear how, or whether, the outflow direction is tied to large-scale core properties. This latter situation is well illustrated by the outflow in L43. The projected outflow direction is clearly perpendicular to the direction of core elongation (Mathieu et al. 1988), and the elongated core is very likely prolate, as demonstrated by Figure 4 of this paper.

5. SUMMARY

The main points presented in this paper are:

(1) Forty-eight line intensity maps of 16 dense cores in dark clouds are compared, based on observations in the 13 mm line of NH_3 and in the 3 mm lines of CS and C^{18}O .

(2) The geometric mean FWHM size of a core map differs from line to line: the average sizes in this sample are 0.15, 0.27, and 0.36 pc for the NH_3 , CS, and C^{18}O lines, respectively. The core maps are similar from line to line in their position on the sky, in their axial ratio, typically 0.5–0.6, and in the direction of their long axes, which are usually aligned within 20° . These points of similarity suggest that elongation is a common characteristic of dense cores.

(3) Core elongation in the present sample does not differ significantly between cores with and without embedded stars: evidently, elongation is a condition prior to star formation,

and not a consequence of star formation. The elongation typical of the present sample is also typical of 19 resolved cores having molecular outflows from embedded stars of low and intermediate mass, studied by Torrelles et al. (1983, 1986) and by Anglada et al. (1989).

(4) The map overlap, elongation, and alignment from line to line in the present sample of low-mass cores constitute closer agreement than is evident between maps of cores associated with OB stars, perhaps due to shocks, ionization, and photochemical effects near OB stars.

(5) The characteristic elongation of dense cores implies that models of equilibrium between self-gravity and isotropic random motions are incomplete, although the typical core appears close to equilibrium if a characteristic size is taken as the radius of an equivalent sphere.

(6) The observed elongation of dense cores in projection is modeled as arising from a group of either prolate or oblate spheroids. The spheroids are identical except for the orientations of their symmetry axes, which are distributed isotropically. To match the typical core, oblate spheroids must be highly flattened, with axial ratio less than 0.1–0.3, while prolate spheroids must have modest elongation, with axial ratio 0.4–0.5.

(7) Six cores (L43, B35, L1251, L234, L1535, and L1400G) are likely to be prolate, because they appear to be integral parts of more extended structures, which in turn are almost certainly prolate because of their extreme elongation. Several other well-known cores are likely to be prolate for similar reasons.

(8) The 10 other cores studied here have less certain shape. They are unlikely to be rotationally flattened, because they generally lack shifts in line center velocity across a map with sufficient magnitude, direction, or both.

(9) Core line widths, map sizes, and column densities are generally consistent with equilibrium models of spheres, rotating or magnetic oblate spheroids, and finite segments of infinitely long prolate cylinders. This comparison alone does not favor one shape over another.

(10) Prolate core geometry may represent an initial condition for some cases of low-mass star formation. This condition cannot be described by a simple model of isolated equilibrium. The six cores in this sample believed to be prolate are generally consistent in line width, column density, and minor axis size with an equilibrium model of an infinitely long prolate cylinder. Their major axis sizes are consistent with estimates of the wavelength of the fastest-growing mode of axial fragmentation of the cylinder. On the other hand, if such fragments were to collapse dynamically, prolate cores formed by this process might not be as prevalent as the observations suggest.

APPENDIX

FORMULATION OF NONSPHERICAL EQUILIBRIUM MODELS TO ALLOW COMPARISON WITH OBSERVED DENSE CORE PROPERTIES

The three nonspherical equilibrium models considered in § 4.3 predict the values of dimensionless variables. These require formulation in terms of other variables in order to compare with quantities derived from observations. This Appendix describes the evaluation of f , n , v_{shift} , and B_{\parallel} , presented in Tables 1B–1D, and compared with observations in § 4.3 and Figure 5. As defined in § 4.3, f sets the coefficient of the linear relation between $(\Delta v)^2/R$ and N in the equilibrium equation (4). The quantity n is the mean number density over a core, within an observationally defined boundary. The quantity v_{shift} is the magnitude of the shift in line-of-sight velocity between opposite ends of the projected long axis of an oblate, rotating core. The line-of-sight component of magnetic field strength, B_{\parallel} , is evaluated at the projected core boundary, for an oblate, magnetized core, and for a finite segment of an infinitely

long prolate cylinder. In this appendix, we give expressions for each of these four quantities in terms of model parameters, the axial ratios p and q , and the quantities Δv and R , derived, respectively, from the observed line width and map size, as described in § 4.3.

The oblate rotating core models of KNMH present measures of core mass, shape, and radius for various values of the ratio of rotational and thermal energy, $\epsilon_{\text{rot}}/\epsilon_{\text{therm}}$, and the ratio of central to boundary density. To obtain f we need expressions for Δv , N , and R . We assume

$$(\Delta v)^2 = 8 \ln 2 c_s^2, \quad (\text{A1})$$

where c_s is the isothermal sound speed. We take

$$N = \frac{M}{\pi m p a^2}, \quad (\text{A2})$$

where M is the mass within the core boundary, N is the mean column density within the projected core boundary, m is the mean molecular mass, and a is the semimajor axis (which for an oblate object is also the projected semimajor axis). The core size

$$R = ap^{1/2} = bp^{-1/2} \quad (\text{A3})$$

is the geometric mean of the projected semimajor and semiminor axes. Then from equation (4), equations (A1)–(A3), and the definitions of KNMH,

$$f = \pi p^{1/2} x_{\text{RM}}, \quad (\text{A4})$$

where x_{RM} is the dimensionless radius-to-mass ratio in the eighth column of KNMH Table 3. The mean density n is obtained from equation (4) and the geometry of an oblate spheroid, giving

$$n = \frac{3p^{3/2}}{32 \ln 2 q f m G} \left(\frac{\Delta v}{R} \right)^2. \quad (\text{A5})$$

Equation (6) is then a special case of equation (A5) with $p = q = 1$. To obtain v_{shift} , we have by definition

$$v_{\text{shift}} = 2v_{\text{rot}} \sin i, \quad (\text{A6})$$

where v_{rot} , the characteristic rotation speed at the core boundary, is

$$v_{\text{rot}} = 2c_s, \quad (\text{A7})$$

following KNMH Figures 7b and 8b. The inclination i between the symmetry axis and the line of sight is given by

$$\sin^2 i = \frac{1 - p^2}{1 - q^2}, \quad (\text{A8})$$

based on the geometry of an ellipse, rotated about its major axis. Combining equations (A1), (A6), (A7), and (A8),

$$v_{\text{shift}} = \left(\frac{2}{\ln 2} \frac{1 - p^2}{1 - q^2} \right)^{1/2} \Delta v. \quad (\text{A9})$$

We assume $p = 0.5$, typical of observed values, and take values of q equal to the inverse of the KNMH parameter f (not to be confused with the parameter f in this paper).

The oblate magnetic core models of TIN present measures of core mass and radius in tabular form, and of core shape and of the ratio of present to initial radius in graphical form. Our estimates are based on TIN Table 3 and Figure 5, for which kinetic and magnetic energies are equal, and for which the dimensionless initial radius x_R equals 4.8. We obtain f using the same procedure as for the oblate rotating core models; in this case

$$f = 4\pi^2 p^{1/2} \frac{x_R y_R}{x_M}, \quad (\text{A10})$$

where x_M is the dimensionless mass in TIN Table 3, and y_R is the dimensionless equatorial radius of the lowest density contour in TIN Figure 5. The mean density over the core is obtained from equations (A5) and (A10). We obtain B_{\parallel} from the assumed equality of kinetic and magnetic energies, according to

$$B_{\parallel} = \left(\frac{2p}{G} \right)^{1/2} \frac{x_R y_R}{8 \ln 2} \frac{(\Delta v)^2}{R} \cos i, \quad (\text{A11})$$

where $\cos i$ is obtained from equation (A8). We estimate q for each of the TIN models from the shape of the outermost density contour in TIN Figure 5. As before, we take $p = 0.5$, typical of observed values.

The magnetized prolate cylinder model of Stodolkiewicz (1963) gives the density structure along a radial line perpendicular to the symmetry axis in terms of the sound speed c_s and the Alfvén speed v_A , each of which is assumed spatially uniform:

$$n(r) = \frac{n_0}{(1 + Ar^2)^2}, \quad (\text{A12})$$

where

$$A = \frac{\pi G m n_0}{2c_s^2 + v_A^2}, \quad (\text{A13})$$

and where n_0 is the density on the cylinder axis. We use equations (A12) and (A13) to obtain the mean column density N within $b_{1/2}$, the projected radius of the half-maximum contour of column density, for a cylinder segment of length $2b_{1/2}/q$, as discussed in § 4.3. The cylinder symmetry axis is inclined at angle i to the line of sight. We assume that the effective line width is given not by equation (A1), but instead by

$$(\Delta v)^2 = 8 \ln 2 \left(c_s^2 + \frac{v_A^2}{2} \right), \quad (\text{A14})$$

in order to be consistent with equation (A13). This assumption implies a magnetic contribution to the line width, as well as to the cloud support. Such a contribution to the line width is not necessary in principle, but appears justified by available evidence (Myers & Goodman 1988). Then

$$f = \frac{p^{1/2} \cos i}{(1 - 2^{-2/3})^{1/2}}. \quad (\text{A15})$$

We assume $p = 0.5$ in accord with the observations in § 2, and $q = 0.4$ in accord with the observations and the model in § 3. In terms of p and q ,

$$\cos^2 i = \frac{p^{-2} - 1}{q^{-2} - 1}, \quad (\text{A16})$$

based on the geometry of an ellipse as for the oblate case (eq. [A8]), but rotated about its minor axis for the present, prolate case. By calculation similar to that of equation (A5), the mean density within $b_{1/2}$ is

$$n = \frac{2 - 2^{1/3}}{8\pi \ln 2 m G p} \left(\frac{\Delta v}{R} \right)^2. \quad (\text{A17})$$

From equations (A12), (A13), and (A14), and the definition of the Alfvén speed v_A , the line-of-sight component of the magnetic field is given by

$$B_{\parallel}^2 = \frac{2^{1/3} - 2^{-1/3}}{\ln 2} \left[\frac{(\Delta v)^2}{8 \ln 2} - c_s^2 \right] \left(\frac{\Delta v}{R} \right)^2 \frac{\cos^2 i}{pG}. \quad (\text{A18})$$

As with equation (A11) for an oblate magnetized core, equation (A18) for a prolate magnetized core gives B_{\parallel} at $b_{1/2}$, the observationally defined core boundary. The field strength is expected to increase toward the center of the core, since v_A is assumed uniform; but an estimate based on the core boundary seems more appropriate to present-day Zeeman measurements, having angular resolution comparable to the core size.

REFERENCES

- Adams, F. C., & Shu, F. H. 1985, *ApJ*, 296, 655
 ———, 1986, *ApJ*, 308, 836
 Anglada, G., Rodriguez, L. F., Torrelles, J. M., Estalella, R., Ho, P. T. P., Canto, J., Lopez, R., & Verdes-Montenegro, L. 1989, *ApJ*, 341, 208
 Arquilla, R., & Goldsmith, P. F. 1986, *ApJ*, 303, 356
 Bastien, P. 1983, *A&A*, 119, 109
 Beichman, C. A., Myers, P. C., Emerson, J. P., Harris, S., Mathieu, R., Benson, P. J., & Jennings, R. E. 1986, *ApJ*, 307, 337
 Benson, P. J. 1983, Ph.D. thesis, Department of Physics, Massachusetts Institute of Technology
 Benson, P. J., & Myers, P. C. 1983, *ApJ*, 270, 589
 Benson, P. J., & Myers, P. C. 1989, *ApJS*, 71, 89 (BM)
 Bohlin, R. C., Savage, B. D., & Drake, J. F. 1978, *ApJ*, 224, 132
 Boss, A. P. 1988, *Comments Ap.*, 12, 169
 Churchwell, E., Winnewisser, G., & Walmsley, C. 1978, *A&A*, 67, 139
 Duvert, G., Cernicharo, J., & Baudry, A. 1986, *A&A*, 164, 349
 Elmegreen, D. M., & Elmegreen, B. G. 1978, *ApJ*, 220, 510
 Fall, S. M., & Frenk, C. S. 1983, *AJ*, 88, 1626
 Fuller, G. A. 1989, Ph.D. thesis, Astronomy Department, University of California, Berkeley
 Genzel, R., & Stutzki, J. 1989, *ARA&A*, 27, 41
 Goodman, A. A., Bastien, P., Myers, P. C., & Menard, F. 1990a, *ApJ*, 359, 363
 Goodman, A. A., Benson, P. J., Fuller, G. A., & Myers, P. C. 1990b, in preparation
 Goodman, A. A., Crutcher, R. M., Heiles, C., Myers, P. C., & Troland, T. H. 1989, *ApJ*, 338, L61
 Heyer, M. H., Snell, R. L., Schloerb, P. F., Strom, S. E., Goldsmith, P. F., & Strom, K. M. 1987, *ApJ*, 321, 855
 Jones, B. F., & Herbig, G. H. 1979, *AJ*, 84, 1872
 Keto, E. R., & Myers, P. C. 1986, *ApJ*, 304, 466
 Kiguchi, M., Narita, S., Miyama, S., & Hayashi, C. 1987, *ApJ*, 317, 830 (KNMH)
 Larson, R. B. 1984, *MNRAS*, 206, 197
 ———, 1985, *MNRAS*, 214, 379
 Lizano, S., & Shu, F. H. 1989, *ApJ*, 342, 834
 Loren, R. B. 1989, *ApJ*, 338, 902
 Mathieu, R. D., Benson, P. J., Fuller, G. A., Myers, P. C., & Schild, R. E. 1988, *ApJ*, 330, 385
 Mouschovias, T. Ch. 1976a, *ApJ*, 206, 753
 ———, 1976b, *ApJ*, 207, 141.
 Myers, P. C., & Benson, P. J. 1983, *ApJ*, 266, 309
 Myers, P. C., & Goodman, A. A. 1988, *ApJ*, 329, 392
 Nakano, T. 1984, *Fund. Cosmic Phys.*, 9, 139
 Ostriker, J. P. 1964, *ApJ*, 140, 1056
 Plambeck, R. L. 1988, in *Galactic and Extragalactic Star Formation*, ed. R. E. Pudritz & M. Fich (Dordrecht: Kluwer), 253
 Rouleau, F., & Bastien, P. 1990, *ApJ*, 355, 172
 Schneider, S., & Elmegreen, B. G. 1979, *ApJS*, 41, 87
 Shu, F. H. 1977, *ApJ*, 214, 488
 Stahler, S. 1983, *ApJ*, 268, 155
 Stodolkiewicz, J. S. 1963, *Acta Astr.*, 13, 30
 Swade, D. A. 1989, *ApJ*, 345, 828
 Terebey, S., Shu, F. H., & Cassen, P. 1984, *ApJ*, 286, 529
 Tomisaka, K., Ikeuchi, S., & Nakamura, T. 1988a, *ApJ*, 326, 208 (TINa)
 ———, 1988b, *ApJ*, 335, 239 (TINb)
 Torrelles, J. M., Ho, P. T. P., Moran, J. M., Rodriguez, L. F., & Canto, J. 1986, *ApJ*, 307, 787
 Torrelles, J. M., Rodriguez, L. F., Canto, J., Carral, P., Marcaide, J., Moran, J. M., & Ho, P. T. P. 1983, *ApJ*, 274, 214
 Zhou, S., Wu, Y., Evans, N. J., Fuller, G. A., & Myers, P. C. 1989, *ApJ*, 364, 168
 Zinnecker, H. 1984, *Ap&SS*, 99, 41
 ———, 1989, in *Proc. ESO Workshop on Low Mass Star Formation and Pre-Main Sequence Objects*, ed. B. Reipurth (Garching: ESO), 447